ADVANCED FUNCTIONAL MATERIALS
www.afm-journal.de

Tuning the Catalytic Preference of Ruthenium Catalysts for Nitrogen Reduction by Atomic Dispersion

Bing Yu, Hao Li, Jai White, Scott Donne, Jiabao Yi, Shibo Xi, Yang Fu, Graeme Henkelman, Hai Yu, Zuliang Chen,* and Tianyi Ma**

Developing cost-effective, high-performance nitrogen reduction reaction (NRR) electrocatalysts is required for the production of green and low-cost ammonia under ambient conditions. Here, a strategy is proposed to adjust the reaction preference of noble metals by tuning the size and local chemical environment of the active sites. This proof-of-concept model is realized by single ruthenium atoms distributed in a matrix of graphitic carbon nitride (Ru SAs/g-C_3N_4). This model is compared, in terms of the NRR activity, to bulk Ru. The as-synthesized Ru SAs/g-C_3N_4 exhibits excellent catalytic activity and selectivity with an NH_3 yield rate of 23.0 μg mg_{cat}^{-1} h^{-1} and a Faradaic efficiency as high as 8.3% at a low overpotential (0.05 V vs the reversible hydrogen electrode), which is far better than that of the bulk Ru counterpart. Moreover, the Ru SAs/g-C_3N_4 displays a high stability during five recycling tests and a 12 h potentiostatic test. Density functional theory calculations reveal that compared to bulk Ru surfaces, Ru SAs/g-C_3N_4 has more facile reaction thermodynamics, and the enhanced NRR performance of Ru SAs/g-C_3N_4 originates from a tuning of the d-electron energies from that of the bulk to a single-atom, causing an up-shift of the d-band center toward the Fermi level.

1. Introduction

Single-atom catalysts (SACs), where metal active sites are atomically dispersed in a host material, have emerged as a new frontier in the area of heterogenous catalysis in the past few years.[1] SACs provide close to 100% metal dispersion and thus can maximize metal utilization. Since SACs have unique catalytic sites, they usually exhibit a distinct catalytic selectivity as compared to their nanoclusters or nanoparticle counterparts.[2] For example, single atomic Pt immobilized in the surface of Ni nanocrystals shows a higher activity and chemoselectivity toward the hydrogenation of 3-nitrostyrene.[3] Isolated Co single-site catalysts anchored on a N-doped porous carbon nanobelt exhibits an excellent catalytic performance for oxidation of ethylbenzene with 98% conversion and 99% selectivity, whereas the Co nanoparticles are essentially inert.[4] Moreover, atomic Ni-anchored covalent triazine framework has a remarkable selectivity for the conversion of CO_2 to CO, with a Faradaic efficiency (FE) of > 90% over the range of −0.6 to −0.9 V versus the reversible hydrogen electrode (RHE).[5] In view of these reported works, it is evident that the size of metal particles is a key factor in determining their catalytic performance, and decreasing the size offers an intriguing opportunity to alter the activity and selectivity of these metal catalysts. SACs, as the limit of size reduction, hold great potential to achieve high activity and selectivity in catalytic reactions.

Recently, the electrocatalytic N_2 reduction reaction (NRR) in aqueous electrolytes for synthesizing ammonia at ambient

Dr. B. Yu, Prof. Z. Chen
School of Environmental Science and Engineering
Fujian Normal University
Fuzhou, Fujian 350007, China
E-mail: zlchen@fjnu.edu.cn
Dr. B. Yu, J. White, Prof. S. Donne, Y. Fu, Dr. T. Ma
Discipline of Chemistry
School of Environmental and Life Sciences
The University of Newcastle
Callaghan, NSW 2308, Australia
E-mail: Tianyi.Ma@newcastle.edu.au
Dr. B. Yu, Y. Fu, Dr. H. Yu
CSIRO Energy
10 Murray Dwyer Circuit, Mayfield West, NSW 2304, Australia
E-mail: hai.yu@csiro.au
The ORCID identification number(s) for the author(s) of this article can be found under https://doi.org/10.1002/adfm.201905665.
Dr. H. Li, Prof. G. Henkelman
Department of Chemistry and the Oden Institute for Computational and Engineering Sciences
Texas Materials Institute
The University of Texas at Austin
105 E. 24th Street, Stop A5300, Austin, TX 78712, USA
Prof. J. Yi
Global Innovative Centre for Advanced Nanomaterials
School of Engineering
The University of Newcastle
Callaghan, NSW 2308, Australia
Dr. S. Xi
Institute of Chemical and Engineering Sciences
A*STAR
1 Pesek Road, Jurong Island, Singapore 627833, Singapore

DOI: 10.1002/adfm.201905665

conditions has gained increasing attention.[6] At present, the industrial-scale production of ammonia still relies heavily on the Haber–Bosch process, which was developed in the early 1900s.[7] This process takes place under harsh conditions (about 450 °C and 300 bar), is energy intensive, and emits massive amounts of greenhouse gases.[8] There are several advantages in electrocatalytic NRR for ammonia synthesis: at first, the required electricity can be supplied by green energy sources, such as solar, tide, wind, etc. In addition, the utilization of aqueous electrolytes has the potential of achieving the simplicity and low cost of this process, because the solvent water can directly serve as the hydrogen source.[9] Moreover, it has added benefits, such as modularity, scalability, and on-site, on-demand generation, which enables ammonia production in remote areas.[10]

Dispersion of metal in the form of single or a few metal atoms as actives sites on a suitable substrate could be an effective strategy to achieve facile ammonia synthesis.[9,11] So far, a variety of single-atom electrocatalysts for NRR has been reported, including Ru single atoms distributed on nitrogen-doped carbon which shows a high and stable NH_3 production rate of 3.665 mg_{NH3} h^{-1} mg_{Ru}^{-1} at –0.21 V versus RHE,[11a] single Mo atoms anchored to nitrogen-doped porous carbon which achieves an NH_3 yield rate (34.0 μg mg_{cat}^{-1} h^{-1}) with the FE of 14.6% at –0.3 V versus RHE,[11b] and Au single sites stabilized on hierarchical nitrogen-doped porous noble carbon which affords a stable NH_3 yield of 2.32 μg h^{-1} with the FE of 12.3% at –0.20 V versus RHE.[11c] Summary of recent reported SACs-based NRR at the mild conditions is given in **Table 1**. However, the synthesis of SACs remains challenging because the high surface free energy of individual metal atoms drives metal aggregation toward nanoclusters or nanoparticles.[1b] Therefore, a suitable substrate that can strongly interact with noble metal clusters is needed to avoid metal aggregation. In recent years, 2D graphitic carbon nitride (g-C_3N_4) has been found to be a superior substrate for supporting catalysts, because it contains a high content of pyridine-like nitrogen which can provide abundant electron lone pairs for anchoring metal ions within its ligands.[12] The application of g-C_3N_4 as a substrate to support noble-metal SACs can offer two obvious advantages: 1) noble-metal atoms are stabilized by g-C_3N_4 in their neutral state which can facilitate catalytical activity[12c] and 2) the outstanding chemical stability facilitates g-C_3N_4 acts as a robust substrate for noble-metal catalysts.[13] In addition, noble-metal catalysts atomically dispersed on the g-C_3N_4 not only maximize the efficiency of these noble metal atoms in terms of cost, but also they will have high electrocatalytic activity and selectivity due to the high ratio of low-coordinated metal atoms. For these reasons, we study g-C_3N_4-supported noble-metal SACs as candidate electrocatalysts for NRR under ambient conditions.

Herein, we developed a new type of NRR catalyst by incorporating Ru single atoms (Ru SAs) into g-C_3N_4, to form the hybrid material (Ru SAs/g-C_3N_4) which was then supported on a free-standing copper foam (CF) to make an electrode for electrocatalytic NRR in strong alkaline electrolytes under ambient conditions. In this electrocatalytic NRR system, the highly conductive CF was utilized to compensate for the semiconducting property of g-C_3N_4. Moreover, the competitive hydrogen evolution reaction (HER) is expected to be suppressed in the strong alkaline electrolyte. In this work, the Ru SAs/g-C_3N_4 exhibited high NRR activity, yielding an NH_3 production rate of 23.0 μg mg_{cat}^{-1} h^{-1} and an FE as high as 8.3% at 0.05 V versus RHE under room temperature and ambient pressure in 0.5 M NaOH electrolyte. These results are superior to that of CF-Ru nanoparticles (Ru NPs). Our catalytic modeling and density functional theory (DFT) calculations indicate that the relatively high activity and selectivity of NRR at single-atom Ru is due to an up-shift of the d-electron energies from Ru bulk to a Ru single atom, which in turn tunes the reaction thermodynamics of NRR to be more favorable.

Table 1. Summary of heterogenous SACs for NRR at mild conditions.

Catalyst	Electrolyte	NH_3 yield	FE [%]	Potential (V vs RHE)
SA-Mo/NPC[11b]	0.1 M KOH	34.0 g h^{-1} mg_{cat}^{-1}	14.6	–0.45
ISAS-Fe/NC[14]	0.1 M PBS	62.9 g h^{-1} mg_{cat}^{-1}	18.6	–0.40
Ru/NC[11a]	0.1 M HCl	3.67 mg h^{-1} mg_{Ru}^{-1}	≈7.5	–0.21
Ru SAs/N-C[9]	0.05 M H_2SO_4	120.9 μg h^{-1} mg_{cat}^{-1}	29.6	–0.20
Au SAs-NDPCs[11c]	0.1 M HCl	2.32 μg h^{-1} cm^{-2}	12.3	–0.20
Au_1/C_3N_4[15]	0.005 M H_2SO_4	1.31 μg h^{-1} mg_{Au}^{-1}	11.1	–0.10
FePc/C[16]	0.1 M Na_2SO_4	10.25 μg h^{-1} mg_{cat}^{-1}	10.50	–0.30
Fe-N/C-CNTs[17]	0.1 M KOH	34.83 μg h^{-1} mg_{cat}^{-1}	9.28	–0.20
Fe_{SA}-N-C[18]	0.1 M KOH	7.48 μg h^{-1} mg_{cat}^{-1}	56.55	0.00

2. Results and Discussion

2.1. Materials Synthesis and Characterization

The synthesis of CF-Ru SAs/g-C_3N_4 can be divided into several steps. As shown in **Figure 1**a, the melamine and $RuCl_3$ was first well-mixed in a water solution via magnetic stirring and then dried overnight at 80 °C. Next, the sample was further heat-treated at 600 °C for 6 h under the N_2 atmosphere. Finally, the acid-etched CF was immersed in the Ru SAs/g-C_3N_4 ink with the aid of the Nafion binder to obtain CF-Ru SAs/g-C_3N_4.

The morphology and microstructure of as-prepared Ru SAs/g-C_3N_4 was examined by scanning electron microscopy (SEM). Figure 1b displays a representative SEM image of g-C_3N_4. For a clearer illustration of the morphology of the as-prepared Ru SAs/g-C_3N_4, we also synthesized the pure g-C_3N_4 using the same method described above for the Ru SAs/g-C_3N_4 synthesis without the addition of $RuCl_3$ for comparison. The successful synthesis of pure g-C_3N_4 was confirmed by X-ray diffraction (XRD; Figure S1, Supporting Information), which exhibited two broad peaks at 12.1° and 27.3°, and these two diffraction peaks were attributed to the (100) and (002) facets of g-C_3N_4, respectively.[12a] Considering that g-C_3N_4 is a semiconductor, its optical band gap can be estimated by a Tauc plot; details of this calculation can be found in the literature.[19] Figure S2 (Supporting Information)

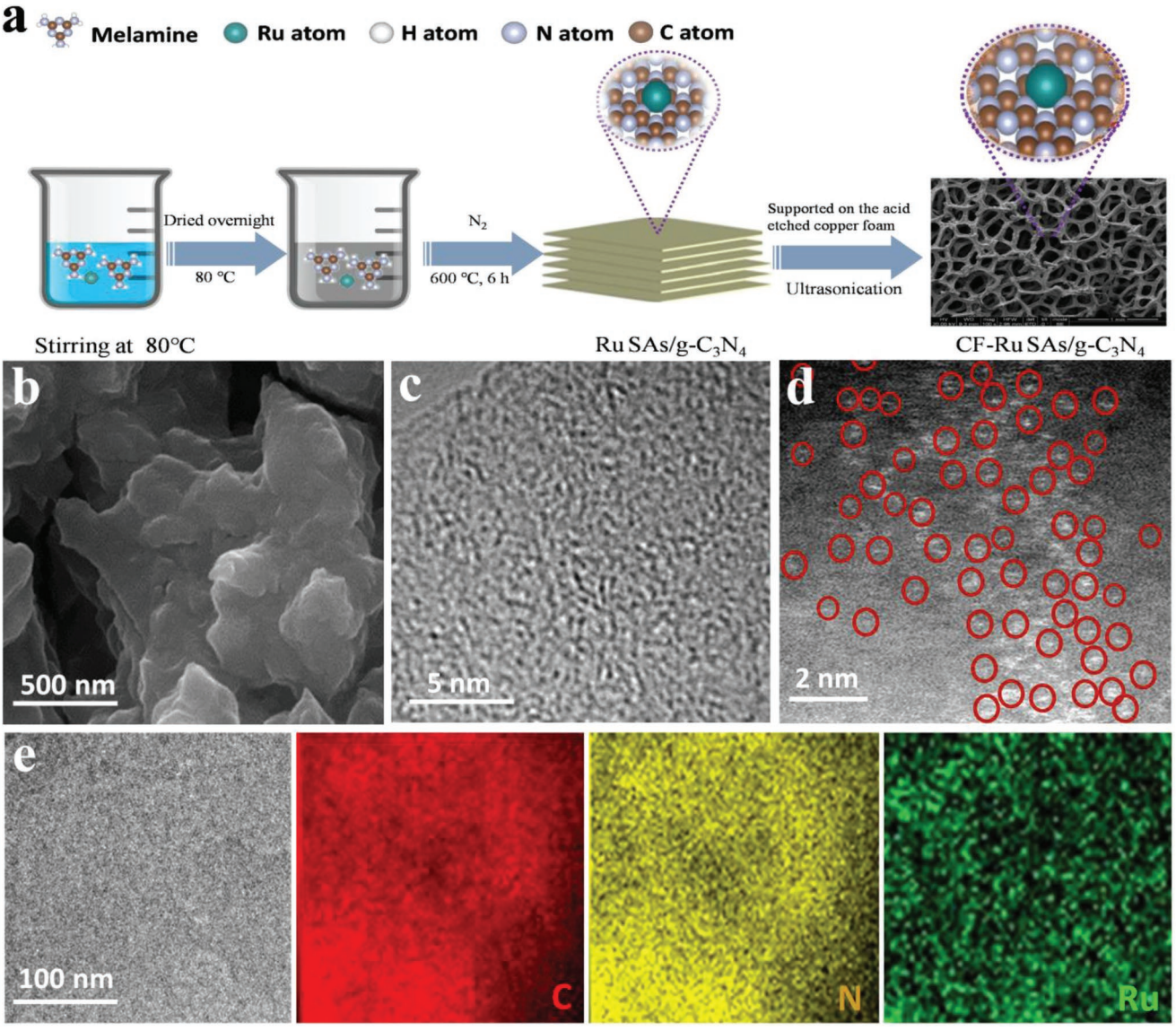

Figure 1. a) Schematic illustration of the synthesis process of CF-Ru SAs/g-C_3N_4. b) A typical SEM image of Ru SAs/g-C_3N_4. c) HRTEM image of Ru SAs/g-C_3N_4. d) HAADF-STEM image of Ru SAs/g-C_3N_4. e) HAADF-STEM image and corresponding EDS elemental mapping results for Ru SAs/g-C_3N_4.

shows the band gap energy of the as-prepared g-C_3N_4 was determined to be 2.75 eV, and the value determined here was in accordance with that of pure C_3N_4, which provides further evidence of the successful synthesis of g-C_3N_4. Furthermore, the observed morphology of pure g-C_3N_4 by SEM was consistent with that of the as-prepared Ru SAs/g-C_3N_4 (Figure S3, Supporting Information). The transmission electron microscopy (TEM) image of the as-prepared Ru SAs/g-C_3N_4 in Figure S4 (Supporting Information) exhibited the typical 2D lamellar structure of g-C_3N_4,[20] moreover, the C/N molar ratio of the as-prepared Ru SAs/g-C_3N_4 measured by X-ray photoelectron spectroscopy (XPS) was about 0.73, close to the theoretical value of 0.75 (Figure S5, Supporting Information). In addition, the XRD was employed to characterize the as-prepared Ru SAs/g-C_3N_4 (Figure S6, Supporting Information), and it was found that Ru SAs/g-C_3N_4 also exhibited two characteristic peaks of pure g-C_3N_4. Although the as-prepared Ru SAs/g-C_3N_4 had a lower crystallinity compared to the pure g-C_3N_4 due to the existence of Ru species, it was still crystalline based on its XRD pattern. These results confirm the formation of g-C_3N_4 within the as-prepared Ru SAs/g-C_3N_4. The high-resolution TEM (HRTEM) photograph of the as-prepared Ru SAs/g-C_3N_4 did not reveal the presence of Ru nanoparticles (Figure 1c), but the existence of Ru in the as-prepared Ru SAs/g-C_3N_4 was confirmed by energy-dispersive X-ray spectroscopy (EDS) analysis (Figure S7, Supporting Information). The high-angle annular dark field scanning transmission electron microscopy (HAADF-STEM) image of the as-prepared Ru SAs/g-C_3N_4 demonstrated that individual Ru atoms were atomically dispersed (Figure 1d), and the corresponding EDS mapping images showed the homogenous distribution of C, N, and Ru over the entire structure (Figure 1e).

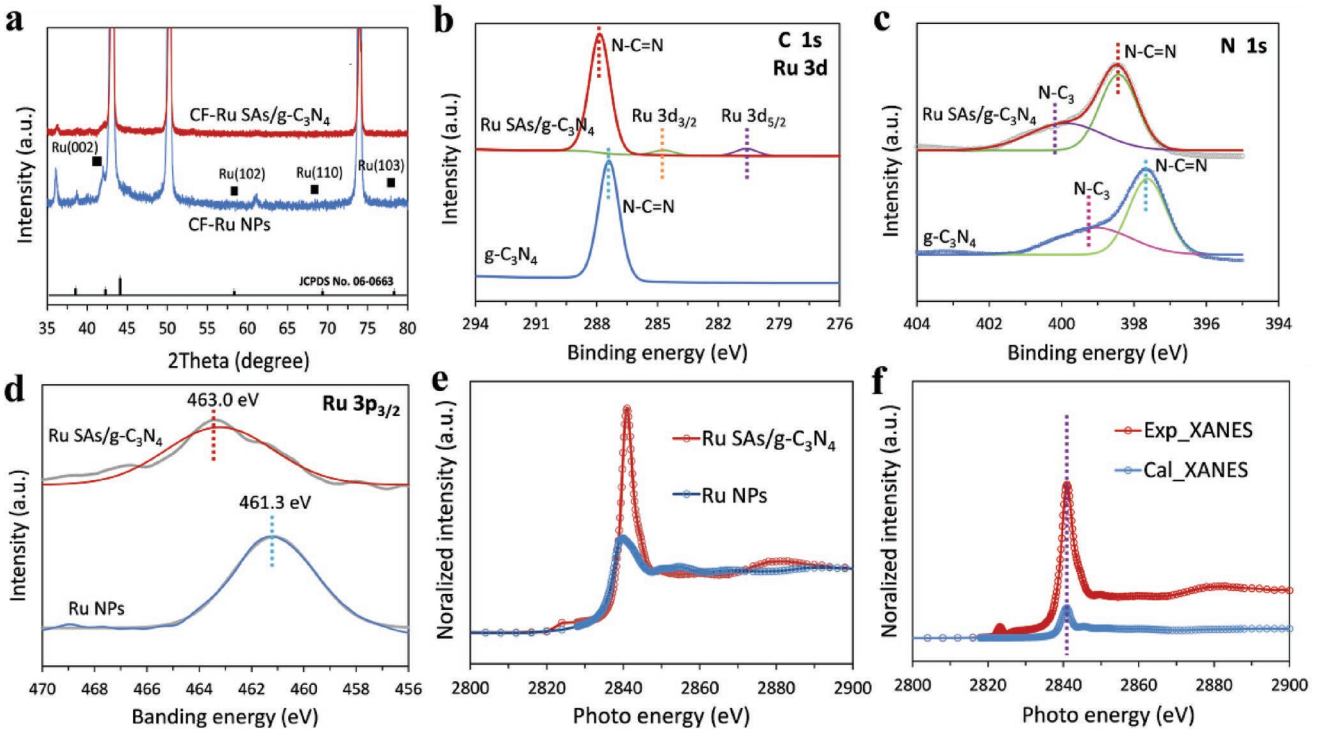

Figure 2. a) XRD patterns for CF-Ru SAs/g-C_3N_4 and CF-Ru NPs. b) High-resolution XPS spectra of C 1s and Ru 3d electrons for Ru SAs/g-C_3N_4 and g-C_3N_4. c) XPS spectra of N 1s electrons for Ru SAs/g-C_3N_4 and g-C_3N_4. d) XPS spectra of the Ru $3p_{3/2}$ for Ru SAs/g-C_3N_4 and Ru NPs. e) Ru L3-edge XANES spectra of Ru SAs/g-C_3N_4 and Ru NPs. f) XANES fitting curve for Ru SAs/g-C_3N_4.

XRD was employed to understand the structure and composition of CF-Ru SAs/g-C_3N_4 and CF-Ru NPs. As shown in **Figure 2**a, the XRD pattern of CF-Ru NPs showed known diffraction peaks including (002), (102), (110), and (103), which can be indexed to a hexagonal-close-packed Ru crystals (JCPDS No. 06–0663).[21] However, these characteristic peaks of the Ru crystal structure were absent in the XRD pattern of CF-Ru SAs/g-C_3N_4, indicating that Ru nanoparticles were not formed in Ru SAs/g-C_3N_4. The XPS spectra of Ru SAs/g-C_3N_4 and pure g-C_3N_4 are shown in Figure S5 (Supporting Information), and it was observed that three peaks appeared at 288, 399, and 534 eV, corresponding to the C 1s, N 1s, and O 1s electrons, respectively. Moreover, the presence of Ru 3d electrons was confirmed by the XPS analysis of the Ru SAs/g-C_3N_4, with Ru atom percentage of 0.6%, indicating that some Ru metal was incorporated into the g-C_3N_4 matrix. Figure 2b shows the XPS spectra of the C 1s for Ru SAs/g-C_3N_4 and pure g-C_3N_4, and only one strong peak appeared at 287.4 eV in pure g-C_3N_4, which can be assigned to the sp^2-hybridized carbon in N−C=N.[19] For Ru SAs/g-C_3N_4, the peak associated with N−C=N was shifted positively to 288.0 eV, which suggested that the electron density of the sp^2 C of g-C_3N_4 was reduced, likely due to charge transfer from g-C_3N_4 to the Ru centers.[22] In addition, for Ru SAs/g-C_3N_4, a doublet at 280.9 and 285.1 eV was identified, which agreed well with the $3d_{5/2}$ and $3d_{3/2}$ electrons of Ru ions in Ru-N moieties, indicating that Ru ions were successfully incorporated into the g-C_3N_4 matrix via Ru-N coordination bonds.[22a] Figure 2c shows the N 1s spectra for Ru SAs/g-C_3N_4 and pure g-C_3N_4, and two subpeaks can be resolved in these two samples. As for g-C_3N_4, a strong peak at 397.8 eV was assigned to the sp^2-hybridized pyridinic nitrogen in N−C=N, and another peak at 399.6 eV corresponded to sp^3-hybridized tertiary nitrogen in N-C_3.[22a,23] For Ru SAs/g-C_3N_4, it was found that the N−C= peak was clearly blueshifted to 398.5 eV, due to charge transfer from g-C_3N_4 to the Ru centers. Figure 2d shows the XPS spectra of the Ru $3p_{3/2}$ for Ru SAs/g-C_3N_4 and Ru NPs, and a peak was found at 461.3 eV corresponding to the metallic Ru appeared in the XPS spectra of Ru NPs, while the peak of the metallic Ru was absent in the XPS spectra of the as-prepared Ru SAs/g-C_3N_4 but a peak at 463.0 eV corresponding to the oxidized Ru.[9] These results confirm the absence of crystalline Ru in Ru SAs/g-C_3N_4, and that Ru atoms in Ru SAs/g-C_3N_4 are atomically dispersed. In addition, the microstructures of the Ru SAs/g-C_3N_4 and pure g-C_3N_4 were investigated by Fourier-transform infrared spectroscopy (FT-IR). As shown in Figure S8 (Supporting Information), several strong peaks in the 1200–1650 cm^{-1} region were assigned to the characteristic stretching modes of CN heterocycles within g-C_3N_4 molecules,[24] and a slight blue-shift of these peaks was observed for Ru SAs/g-C_3N_4. These results are also indicative of the successful incorporation of Ru into the g-C_3N_4 substrate. The X-ray absorption near-edge spectroscopy (XANES) was employed to further understand the electronic and coordination structures of Ru SAs/g-C_3N_4. Figure 2e shows the Ru L_3-edge XANES profiles for Ru SAs/g-C_3N_4 and Ru NPs. It was found that Ru SAs/g-C_3N_4 exhibited a distinct energy absorption edge profile in a range between 2830 and 2850 eV compared with Ru NPs. The position of the white line in the Ru L_3-edge of Ru NPs

was located at 2839.6 eV, which was in line with that of reported Ru powder.[25] In contrast, the position of the white line in the Ru L_3-edge of Ru SAs/g-C_3N_4 was located at 2841.0 eV, which matched well with that of reported highly charged Ru species.[25] In addition, the intensity of the pre-edge feature of Ru L_3-edge spectra is indicative for the covalency of the ligand-metal bonds, and a larger intensity of the white line corresponds to a higher oxidation state of Ru. The Ru L_3-edge spectrum of Ru SAs/g-C_3N_4 exhibited a more prominent pre-edge line than Ru NPs, originating from the highly covalent bonding of Ru-N in Ru SAs/g-C_3N_4. To gain further insights into the accurate structure of Ru SAs/g-C_3N_4, a least-squares XANES fitting was performed, and the used structure parameters of Ru SAs/g-C_3N_4 were obtained from our following DFT calculations. As shown in Figure 2f, it was found that the position of the white line in the fitting curve of Ru SAs/g-C_3N_4 well matched with the measured XANES result, which further confirmed that the Ru atoms in Ru SAs/g-C_3N_4 were coordinated by N donor atoms from g-C_3N_4 and thereby isolated to form an atomic dispersion.

The results from the above material characterizations demonstrate that g-C_3N_4 is an excellent substrate for the deposition and fixation of Ru single atom sites. The incorporation of Ru ions into the g-C_3N_4 through Ru-N coordination bonds prevented the aggregation of Ru atoms and led to the formation of Ru single-atom sites. The structure of the single-atom Ru sites will be described in more detail through our calculations (Section 2.3).

2.2. Catalytic Nitrogen Reduction

To evaluate the electrocatalytic NRR activities of CF-Ru SAs/g-C_3N_4 under ambient conditions, several electrochemical tests were performed in N_2-saturated 0.5 M NaOH electrolyte, such as linear sweep voltammetry (LSV) and chronoamperometry. All tests were performed in a two-compartment cell separated by a proton conductive cation exchange membrane (Nafion 115), in which the protons (H^+) can react with N_2 to form ammonia over the catalyst. The experimental apparatus for the electrocatalytic NRR is shown in Figure S9 (Supporting Information). At first, the LSV curves for CF-Ru SAs/g-C_3N_4 in Ar- or N_2-saturated 0.5 M NaOH solutions were measured to verify the source of ammonia (**Figure 3**a). When the applied potential was less negative than –0.3 V versus RHE, and a higher current density in N_2-saturated solution was observed in comparison with that under Ar-saturated solution, this indicates that the electrocatalytic N_2 reduction can be realized by the as-prepared CF-Ru SAs/g-C_3N_4. As the applied potential was set more negative than –0.3 V versus RHE, the current densities in N_2-saturated and Ar-saturated solutions were very close, likely because the HER becomes dominant as compared to the NRR in this system. The Nessler's reagent and ammonia-sensitive selecting electrode methods were carried out independently for the quantitative analysis of ammonia in the electrolyte after 1 h of electrolysis in the presence of continuous Ar bubbling, and a very small amount of ammonia (< 10 ppb) was detected in the electrolyte, which suggested that the contribution of ammonia yield from the catalyst itself, the Nafion-dispersed liquid, and the ambient environment in the lab was almost negligible. Given that N_2H_4 is a possible by-product of the electrocatalytic N_2 reduction, the colorimetric method was employed to examine if N_2H_4 was produced in the current experiments. No N_2H_4 was detected in the electrolyte after 1 h of electrolysis in the presence of continuous N_2 bubbling (Figure S10, Supporting Information), indicating that the as-prepared CF-Ru SAs/g-C_3N_4 has a good selectivity for the NRR.

Figure 3b shows the LSV curves of CF, CF-g-C_3N_4, CF-Ru NPs, and CF-Ru SAs/g-C_3N_4 for electrocatalytic NRR. At all applied potentials, CF had a much lower current density onset potential than that of CF-g-C_3N_4, CF-Ru NPs, and CF-Ru SAs/g-C_3N_4, which can be attributed to the inert HER activity of CF compared to that of Ru. In addition, a low current density was observed for CF-Ru SAs/g-C_3N_4 at a potential range between –0.3 and 0 V versus RHE, while CF and CF-g-C_3N_4 exhibited no current density within this potential range. This was partially due to the HER activity of Ru and more importantly, due to the ignition of electrocatalytic NRR activity of Ru at low potentials compared to that of CF and CF-g-C_3N_4. Figure 3a also confirmed that electrocatalytic N_2 reduction was realized by this as-prepared CF-Ru SAs/g-C_3N_4 at low potentials. Therefore, it can be inferred here that the Ru in CF-Ru SAs/g-C_3N_4 played the decisive role in the electrocatalytic NRR, while CF and CF-g-C_3N_4 possessed no activity toward the electrocatalytic NRR.

Figure 3c,d shows the FEs and ammonia yield rates of CF, CF-g-C_3N_4, CF-Ru NPs, and CF-Ru SAs/g-C_3N_4 under various applied potentials ranging from 0.05 to –0.6 V versus RHE. The data in these two figures were obtained based on the method of the ion-selective electrode meter. To confirm the reliability of this method for ammonia detection, it was confirmed that a colorimetric method using Nessler's reagent gave consistent results (Figure 3e); and it was also found that the values determined by the colorimetric method were a bit higher than those determined by ion-selective electrode meter. To further confirm this trend, the measurement of several prepared standard ammonia solutions was performed, and the results indeed revealed the same trend as the above experimental results. In addition, the ion-selective electrode meter exhibited a higher accuracy than the colorimetric method in this electrocatalytic NRR system (Figure S11, Supporting Information). As for CF-Ru NPs, and CF-Ru SAs/g-C_3N_4 studied in this work, both of their FEs experienced a gradual decreasing trend as the applied potential increased to a more negative value. In fact, a remarkable increase of the current density was observed with the increase of applied potentials (Figure 3f), which was caused by the predominance of HER at higher overpotentials and thus resulted in the decline of FEs. In addition, there was no ammonia yield for CF, which confirmed that CF has no catalytic activity toward the NRR. The result further confirmed the contribution of ammonia from CF can be negligible. Moreover, the control experiment using CF-g-C_3N_4 was also performed and shown in Figure 3c,d, and it was also found that no ammonia was produced when subtracting the ammonia measured during the Ar control experiment. This indicated that g-C_3N_4 had no catalytic activity toward NRR for the production of ammonia, and the contribution of ammonia yield from the impurities of g-C_3N_4 was also negligible. Compared to CF-Ru NPs, CF-Ru SAs/g-C_3N_4 exhibited higher FEs at all tested potentials, and the highest FE of CF-Ru SAs/g-C_3N_4 was 8.3% at 0.05 V versus RHE

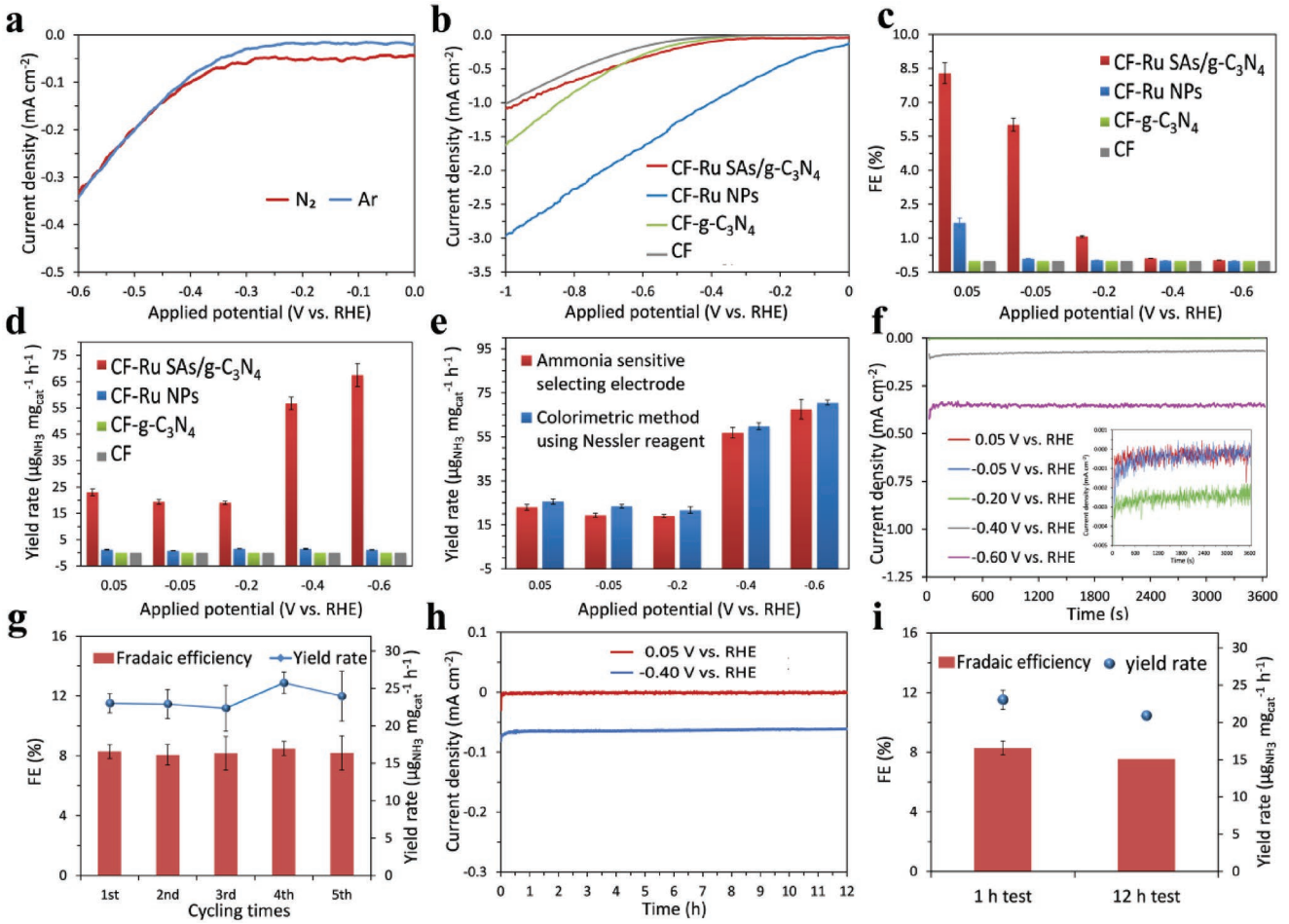

Figure 3. a) LSV curves of CF-Ru SAs/g-C_3N_4 electrode in a N_2 and Ar saturated aqueous solution of 0.5 M NaOH. b) LSV curves of CF, CF-g-C_3N_4, CF-Ru NPs, and CF-Ru SAs/g-C_3N_4 electrodes in a N_2 saturated aqueous solution of 0.5 M NaOH. c) FEs and d) ammonia yield rates at different potentials ranging from 0.05 to –0.60 V versus RHE. e) Comparison of the ammonia-sensitive selecting electrode and Nessler reagent-based colorimetric method for the quantitative analysis of ammonia yield rate. f) Chronoamperometry results at the corresponding potentials. g) FEs and ammonia yield rates during five consecutive cycles. h) Chronoamperometry results at the 0.05 and –0.40 V versus RHE. i) FEs and ammonia yield rates within 1 and 12 h tests.

(Figure 3c), which is 4.9 times that of CF-Ru NPs (FE_{NH3} 1.7%). Moreover, the ammonia yield rate was normalized based on the weight of the catalysts and the NH_3 yield rate of CF-Ru SAs/g-C_3N_4 was 23.0 μg mg_{cat}^{-1} h^{-1} at 0.05 V versus RHE (Figure 3d). As far as we know, the NH_3 yield rate and FE that the CF-Ru SAs/g-C_3N_4 achieved at 0.05 V versus RHE are comparable to recently reported NRR electrocatalysts. For example, Kong et al. reported that WO_3 nanosheets rich in oxygen vacancies afforded an NH_3 yield of 17.28 μg h^{-1} mg_{cat}^{-1} and an FE of 7.0% at –0.3 V versus RHE.[26] Chu et al. reported that NiO nanodots supported on graphene exhibited an NH_3 yield of 18.6 μg h^{-1} mg_{cat}^{-1} and an FE of 7.8% at –0.7 V versus RHE.[27] Luo et al. found that the MXene nanosheets achieved a stable NH_3 yield rate of 4.72 μg h^{-1} and an FE of 4.62% at –0.1 V versus RHE.[28] However, an ultralow applied potential (0.05 V vs RHE) was used for CF-Ru SAs/g-C_3N_4 here that makes it one of the most active and selective electrocatalysts for NRR at ambient conditions. Although the highest ammonia yield rate as high as 67.5 μg mg_{cat}^{-1} h^{-1} was achieved at –0.6 V versus RHE, the FE for CF-Ru SAs/g-C_3N_4 at –0.6 V versus RHE was extremely low. A plausible explanation is that N_2 has a low solubility in water, and the electrocatalytic NRR in this system was in a N_2 diffusion-controlled mode. At higher negative potentials, the HER was dominant,[11a] so the surface of CF-Ru SAs/g-C_3N_4 was mainly occupied by the evolving hydrogen molecules which would block the mass transfer of N_2 to the surface of CF-Ru SAs/g-C_3N_4, and thus limit the electrocatalytic NRR activity.

The stability of the CF- Ru SAs/g-C_3N_4 for electrocatalytic N_2 reduction was evaluated by consecutive recycling electrolysis at 0.05 V versus RHE. The ammonia yield rate and the current efficiency remained stable during five consecutive cycles (Figure 3g), indicating the high stability of CF-Ru SAs/g-C_3N_4 for electrochemical N_2 reduction. Additionally, the stability of CF-Ru SAs/g-C_3N_4 was also assessed by scanning at a constant potential of 0.05 and –0.4 V versus RHE for 12 h. The current density presented no obvious change at these two potentials (Figure 3g), and CF-Ru SAs/g-C_3N_4 exhibited unremarkable decay of NH_3 production yield rate and FE at 0.05 V versus RHE during the 12 h potentiostatic test (Figure 3i), indicating that CF-Ru SAs/g-C_3N_4 can effectively produce ammonia over

a long period of time. The characterization for Ru SAs/g-C_3N_4 after cycling by XRD, XPS, and HAADF-STEM has been performed (Figure S12, Supporting Information), and the results confirmed that Ru atoms were still atomically dispersed without the formation of Ru NPs after the stability test. Therefore, the as-prepared CF-Ru SAs/g-C_3N_4 was demonstrated to be a highly stable catalyst for electrochemical N_2 reduction.

To gain more insights to the intrinsic reasons for the high NRR activity of Ru SAs/g-C_3N_4, we performed N_2 temperature-programmed desorption (N_2-TPD) for Ru SAs/g-C_3N_4. As shown in Figure S13 (Supporting Information), Ru SAs/g-C_3N_4 exhibited a peak of N_2-TPD at 650 °C, which was attributed to the chemical adsorption of N_2 on Ru SAs/g-C_3N_4. In fact, the temperature for the N_2-TPD peak of Ru SAs/g-C_3N_4 here was even higher than that of recently reported Ru SAs/N-C,[9] which further suggested the strong binding of N_2 on Ru SAs/g-C_3N_4 and thus facilitated its high NRR activity.

2.3. Theoretical Investigations

To theoretically evaluate the reactivity of the NRR at the single-atom Ru on g-C_3N_4, DFT calculations were performed on Ru SAs/g-C_3N_4 (**Figure 4**a). Similar to the mechanisms found by Back and Jung,[29] five possible NRR pathways were evaluated here: N_2 associative and dissociative pathways, as well as pathways through the dissociation of NNH_2, $HNNH_2$, and H_2NNH_2. It can be seen from Figure 4a that the dissociation of N_2 is the least favorable pathway due to the rate-limiting N_2 dissociation step (2.34 eV). For the other pathways, the potential-determining step is the formation of NNH* (0.62 eV). It should be noted that though the desorption of NH_3* is endothermic, the protonation of NH_3* would form NH_4^+ in solution, which is expected to be a favorable step.[30] Therefore, except the N_2 dissociative pathway, all other pathways are thermodynamically exothermic at an appropriate applied potential. To model the Ru bulk structure, as studied in our experiments, similar NRR pathways on Ru(0001) were evaluated with DFT (Figure 4b). It can be clearly seen that though the formation of NNH* and 2N* are exothermic, adsorption of N_2 on Ru(0001) is the rate-determining step and this step is not electrochemically tuned with an applied potential. Therefore, as compared to Ru(0001), Ru SAs/g-C_3N_4 is predicted to be more active for the NRR. The significant adsorption geometries of the hydrogenated-N_2 species can be found in Figure S14 in the Supporting Information.

To evaluate the efficiency of NRR, DFT was performed to evaluate the competing HER on bare g-C_3N_4, Ru SAs/g-C_3N_4, and Ru(0001) (Figure 4c). It can be seen from the hydrogen evolution step that a bare g-C_3N_4 has facile HER but is unfavorable for NRR since it cannot stabilize N_2 adsorption in our calculations so that the NRR activity should come from the Ru sites. Figure 4c shows that HER on Ru(0001) is ≈0.19 eV more facile than on Ru SAs/g-C_3N_4 for the hydrogen evolution, indicating that HER is relatively difficult on under-coordinated surface sites due to the strong binding of H. Also, the adsorption free energy of H is more exothermic than that of N_2 at Ru(0001) (Figure 4b), while these two binding energies at Ru SAs/g-C_3N_4 are similar. Our calculations clearly indicate that H adsorption would significantly reduce the number of NRR active sites on Ru(0001), while this H poisoning effect is much less significant at Ru SAs/g-C_3N_4, leading to selectivity for the NRR. Since our experiments were under alkaline conditions, we also evaluated the kinetic barrier of the water dissociation step, as shown in the inset of Figure 4c. It was found that both Ru SAs/g-C_3N_4 and Ru(0001) have a high dissociation barrier (0.82 and 0.84 eV, respectively), while no stable dissociation configuration was found on the bare g-C_3N_4. This clearly indicates that in addition to the less significant H poisoning effect found on Ru SAs/g-C_3N_4, the slow kinetic of water dissociation also hinders HER on all these evaluated sites. It should be noted that the tunability of adsorbate bindings is particularly important for tuning the activity of a specific catalytic site.[31] As discussed, both the H and N_2 binding energies are tuned stronger for the systems with single-atom Ru. For bulk Ru, the activity is dominated by nondefected Ru sites (e.g., the energetically favorable (0001) surface) which promotes HER and inhibits NRR. It should be mentioned that HER on both Ru SAs/g-C_3N_4 and Ru(0001) (Figure 4c) should be more facile than NNR (Figure 4a,b), which is in good agreement with our experimental result that the HER selectivity is higher than NRR in all the catalysts evaluated (Figure 3c). To understand the strengthened bindings of H and N_2 at Ru SAs/g-C_3N_4, the projected density of states (PDOS) of the d-electrons of a Ru site of Ru SAs/g-C_3N_4 and the Ru(0001) surface were calculated (Figure 4d). Interestingly, with different atomic environments, these two Ru sites show very different PDOS distributions. Their calculated d-band centers (average energy of the d-electrons) indicate that Ru SAs/g-C_3N_4 has a d-band center closer to the Fermi level, which in turn leads to stronger adsorbate binding energies than the Ru bulk surface.[32] Furthermore, the calculated charge density difference of Ru doped on g-C_3N_4 shows that the doping of Ru leads to significant electronic rearrangement of both the single-atom Ru and g-C_3N_4 (Figure 4d, inset), suggesting that the Ru-N bonding tunes the electronic properties of the system.

3. Conclusions

In summary, we have developed a new g-C_3N_4-supported Ru single-atom electrocatalyst and demonstrated the catalyst to be highly active toward electrochemical NRR in strong alkaline electrolytes at ambient conditions. The as-synthesized Ru SAs/g-C_3N_4 afforded an NH_3 yield rate of 23.0 μg mg_{cat}^{-1} h^{-1} and an FE of 8.3% at 0.05 V versus RHE. As revealed by the spectroscopic studies and electrochemical NRR tests, the outstanding NRR activity of Ru SAs/g-C_3N_4 was attributed to the formation of Ru single sites supported on the g-C_3N_4. Furthermore, DFT calculations showed that a single-atom Ru supported on g-C_3N_4 possesses more facile NRR reaction activity due to its stronger N_2 adsorption and reduced H poisoning at the reactive sites, in good agreement with the measured catalytic activity and selectivity.

4. Experimental Section

Chemicals: Ruthenium(III) chloride ($RuCl_3$, Ru content 45–55%), hydrogen peroxide solution (H_2O_2, reagent grade, 30 wt%), sulfuric acid

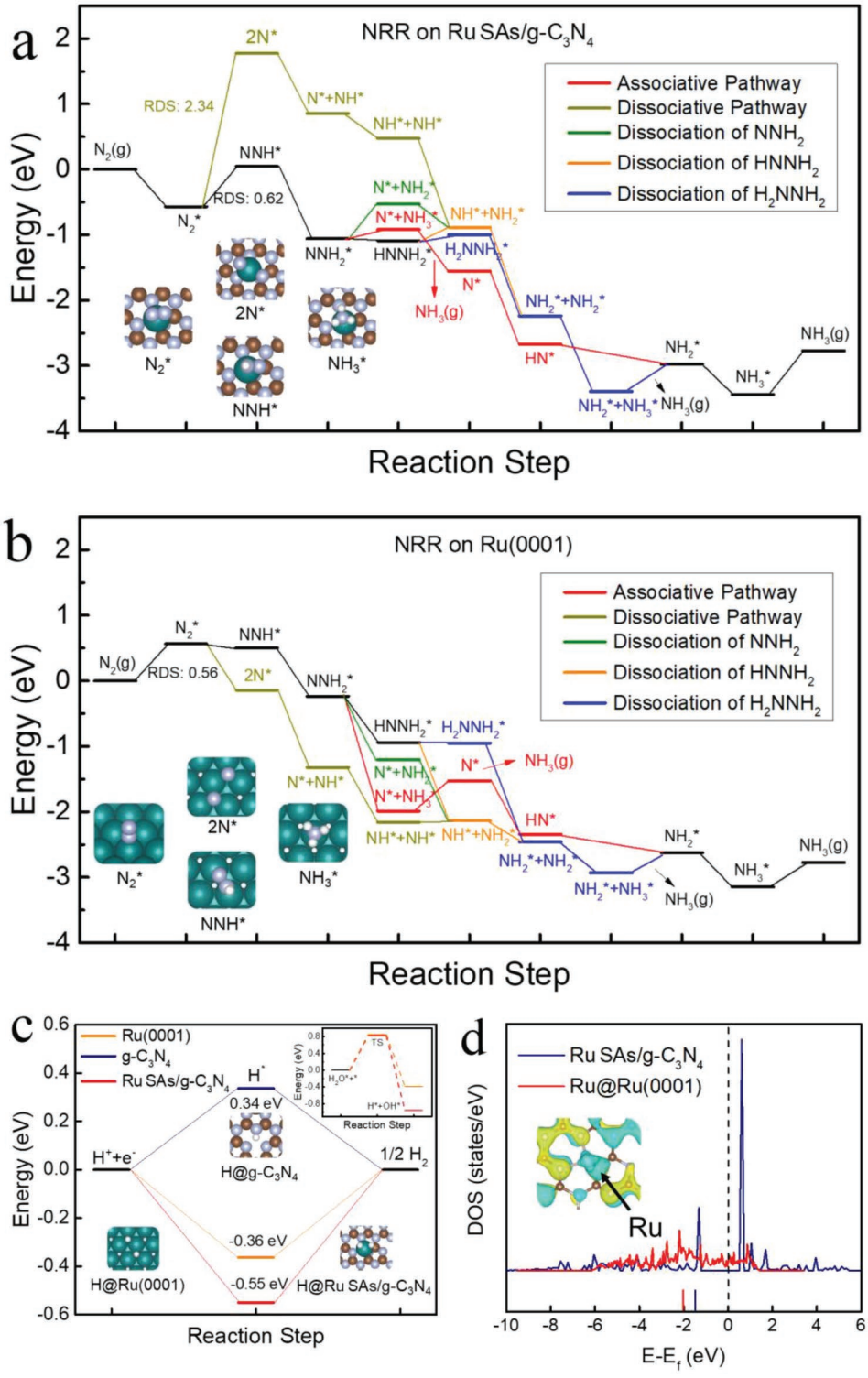

Figure 4. Reaction free energy pathways of NRR on a) Ru SAs/g-C_3N_4 and b) Ru(0001). The NH_3* will then be protonated and form NH_4^+ in solution (not shown). Insets show the adsorption geometries of N_2*, 2N*, NNH*, and NH_3*. Teal, blue, brown, and white spheres represent Ru, N, C, and H atoms, respectively. Other important adsorption geometries can be found in **Figure S14** in the Supporting Information. c) Reaction free energy pathways of HER on Ru SAs/g-C_3N_4, g-C_3N_4, and Ru(0001). Insets show the reaction pathways of water dissociation and the adsorption geometries of H*. Teal, blue, brown, and white spheres represent Ru, N, C, and H atoms, respectively. d) Calculated projected density of states (PDOS) of d-electrons of a Ru atom of the Ru SAs/g-C_3N_4 and Ru(0001) surface. Black dashed line represents the Fermi level. Blue and red horizontal bars represent the d-band center of the Ru site at Ru SAs/g-C_3N_4 and Ru(0001) surface, respectively. Inset shows the calculated charge density difference of the doping of Ru SAs at a g-C_3N_4.

(H_2SO_4, 99.999%), hydrochloric acid solution (HCl, 32 wt% in H_2O), sodium hydroxide solution (NaOH, reagent grade, 10 M in H_2O), Nafion perfluorinated membrane (Nafion 115, thickness 0.005 in.), melamine ($C_3H_6N_6$, 99%), hydrazine hydrate (N_2H_4, 50–60%), Nessler's reagent, potassium sodium tartrate solution, 4-(dimethylamino)benzaldehyde (reagent grade, 99%), and sodium borohydride powder ($NaBH_4$, reagent grade, ≥98.0%) were purchased from Sigma-Aldrich. All chemicals were used without further purification. Argon gas (99.99%) and nitrogen gas (99.99%) were purchased from Coregas Australia, and all solutions were prepared with deionized water.

Synthesis of g-C_3N_4, CF- Ru SAs/g-C_3N_4, CF-g-C_3N_4, and CF-Ru NPs: As a substrate material in this study, g-C_3N_4 was prepared by thermal polymerization, where melamine served as the precursor, and a tube furnace was used to heat the material to the polymerized phase. The melamine precursor was placed in an alumina boat and covered in aluminium foil with small holes to allow for the passing of nitrogen gas at 50 mL min^{-1}. This was done in an effort to prevent excessive material loss through melamine vaporization and NH_3 condensation and to retain as much of the g-C_3N_4 as possible. The heating process was as follows: from room temperature the sample was heated to 600 °C over 6 h and held at 600 °C for 4 h then cooled back to room temperature over a further 4 h.

Ru SAs/g-C_3N_4 was synthesized through several steps. The total melamine plus $RuCl_3$ was made up to be 10 g with the weight percentage of $RuCl_3$ of 7.5%. The mixture was added to water at 80 °C and stirred and continuously heated to maintain the temperature until the water had evaporated. The mixture was then dried overnight in an oven at 80 °C to slowly remove any remaining water. The samples were then mixed via mortar and pestle to provide further homogeneity and placed in a tube furnace and heat treated using the same method previously discussed for the pure g-C_3N_4 synthesis. Subsequently, the acid-etched CF was immersed in the obtained Ru SAs/g-C_3N_4 ink with the aid of the Nafion binder, and the resulting CF-Ru SAs/g-C_3N_4 was dried at room temperature overnight, and the loading amount of Ru SAs/g-C_3N_4 was determined by the weight difference between the acid-etched CF with and without the loading of the catalyst. The synthesis of the control material CF-g-C_3N_4 was the same as the CF-Ru SAs/g-C_3N_4 except the used ink was pure g-C_3N_4. The CF-Ru NPs was synthesized using a facile ultrasonic-assisted chemical reduction method. First, the acid-etched CF was inserted in 20 mL $RuCl_3$ solutions (20 mmol L^{-1}), which was placed in an ultrasonic water bath with the temperature kept at 50 °C for 1 h and the excessive $NaBH_4$ was slowly added into the above mixture. The obtained CF-Ru NPs was then taken out from the solution and dried at room temperature overnight.

Material Characterization: SEM images were obtained on a Zeiss Sigma VP FESEM instrument operating at 3 kV after sputtering with gold, and EDS investigations were conducted to gather information regarding weight% of metal present and uniformity of metal dispersion and coordination. TEM conducted on a JEOL-2100 HRTEM instrument operating at 200 kV along with the EDS detector JEM-2300 was used. The HAADF-STEM images were recorded using a FEI Titan G2 80–300 microscope at 300 kV equipped with a probe corrector. EDS imaging was conducted with a FEI Titan Themis 80–200 microscope equipped with a SuperX detector. The crystallinity of obtained samples was characterized by XRD patterns, recorded on a Bruker D8 advance X-ray diffractometer with Cu Kα radiation. XPS measurements were performed using a Thermo Scientific K-Alpha$^+$ X-ray photoelectron spectrometer. All samples were analyzed using a microfocused, monochromated Al-K_α X-ray source (1486.68 eV; 400 µm spot size). The K-Alpha$^+$ charge compensation system was employed during analysis to prevent any localized charge buildup. FT-IR was recorded on a Bruker Vertex 70 spectrophotometer. XANES measurements at the Ru L_3-edge were carried out at room temperature at Singapore Synchrotron Light Source using the transmission mode. A Si(111) monochromator was used for varying the energy in the desired range.

Electrochemical Measurements: Prior to N_2 reduction tests, Nafion 115 membranes were heat-treated in 5% H_2O_2, 0.5 M H_2SO_4, and deionized water for 1 h, respectively. After being rinsed with water thoroughly, the membranes were immersed in deionized water for future use. Electrochemical measurements were performed using an Autolab/PGSTAT302 Potentiostat–Galvanostat (Metrohm Autolab BV, Netherlands), with a gas-tight two-compartment electrochemical cell separated by a piece of Nafion 115 membrane at room temperature. A piece of Pt gauze was used as counter electrode, and a Ag/AgCl/sat. KCl (4 M) electrode was employed as reference electrode. In all measurements, the Ag/AgCl reference electrode was calibrated with respect to RHE. The calibration was performed in the high-purity hydrogen-saturated electrolyte with a Pt foil as the working electrode. Cyclic voltammetry was run at a scan rate of 1 mV s^{-1}, and the average of the two potentials at which the current crossed 0 was taken to be the thermodynamic potential for the hydrogen electrode reaction. In 0.5 M NaOH solution, $E_{RHE} = E_{Ag/AgCl} + 1.008$. The calibration result agreed very well with the result obtained from the theoretical calculation based on the following Nernst equation

$$E_{RHE} = E_{Ag/AgCl} + 0.059 \times pH + 0.205 \quad (0.205 \text{ would be different if another KCl concentration was selected}) \quad (1)$$

LSV tests were performed in N_2- and Ar-saturated solution at a scan rate of 5 mV s^{-1}. All LSV curves were steady-state ones after the working electrodes were scanned several times. The current density was normalized to the geometrical area. Potentiostatic tests were carried out at different potentials ranging from +0.05 to at −0.6 V versus RHE for 1 h at room temperature (≈293 K). Prior to each electrolysis, the work electrode was reduced at a low applied potential (−0.1 V vs RHE) for 30 min. 0.5 M NaOH solution was used as electrolyte, and it was presaturated with N_2 by introducing a pure N_2 gas stream for 1 h. The electrolyte was continuously bubbled with N_2 and was agitated solution with stirring by a magnetic stirrer at ≈150 rpm during each electrolysis experiment.

Quantification of Ammonia: The quantity of the produced NH_3 in the electrolyte was measured by an ion-selective electrode meter (Orion Star A214 Benchtop pH/ISE Meter; Thermo Scientific), and the method could be used to measure the ammonia in aqueous solution that had a concentration of 10 ppm as nitrogen or lower. Four standard ammonia solutions (10, 100, 1000, and 10 000 ppb) were prepared from a stock solution (1000 ppm ammonia as nitrogen standard) for the calibration with the slope in the range of −56 to −60 mV when the standards were between 20 and 25 °C. To minimize the impact of the background of the N_2-saturated electrolyte (0.5 M NaOH) on the quantitative analysis of the produced NH_3, each standard ammonia solution was prepared by the dilution of the stock NH_4Cl solution using the N_2-saturated 0.5 M NaOH solution. Ionic strength adjuster (ISA) was used to provide a constant background ionic strength and adjust the solution pH. ISA must be added to all samples and standards immediately before measurement to prevent ammonia loss, and 80 mL of standard or sample required the addition of 1.6 mL ISA with the stirring thoroughly.

In addition, to test if ammonia escaped from the electrolyte solution, the outlet gas was introduced to an acid bottle for wet scrubbing to collect the possible escaping ammonia. The ion-selective electrode meter was employed to measure the ammonia concentration in the acid wet scrubbing bottle, and the experimental results revealed that no ammonia was detected, suggesting that the ammonia escaping from the electrolyte solution could be negligible.

A colorimetric method using Nessler's reagent for NH_3 detection was also performed to further examine the reliability of the former method, and the test solutions were measured as the absorbance at 420 nm by an UV-vis spectrometer (PerkinElmer Lambda 950). A standard curve of the Nessler's reagent-based colorimetric method for the quantitative analysis of produced ammonia is shown in Figure S15 (Supporting Information). A series of standard ammonia solutions with different concentrations was prepared, and the values determined by Nessler's reagent were almost identical to that of determined by the ion-selective electrode meter within experimental error, suggesting that it was reliable to use the selective electrode meter for the quantitative analysis of the produced NH_3 (Figure S11, Supporting Information).

Quantification of Hydrazine: In addition, the yield of hydrazine in the electrolyte was examined by Watt and Chrisp method. The color reagent was prepared by a mixture of para-(dimethylamino) benzaldehyde (5.99 g), HCl (concentrated, 30 mL), and ethanol (300 mL). The yields of hydrazine in the resulting electrolytes were detected after mixing with the color reagent by measuring the absorbance at 455 nm.

The Calculation of FE and NH_3 Yield: The calculation of FE of NH_3 based on Equation (2)

$$\mathrm{FE} = \frac{3 \times F \times c \times V}{17 \times Q} \tag{2}$$

where F is Faraday constant, V is the total volume of electrolyte in cathodic compartment, Q is the total charge passed through the electrochemical system, and c is the calculated concentration of NH_3. NH_3 yield was also obtained according to Equation (3) as follows

$$\mathrm{NH_3\ yield} = \frac{c \times V}{t \times A} \tag{3}$$

where t is the reaction time, A is the surface area of working electrode, V is the total electrolyte volume in cathodic compartment, and c is the concentration of NH_3.

Calculation of the Equilibrium Potential: A strong alkaline solution was employed as the electrolyte in this work with its pH value as high as 13.69, which was much greater than the p*K*a value for NH_4^+ (9.24). In this case, the newly produced ammonia gas formed a type of coordination with water, as shown in Equation (4)

$$\mathrm{N_2(g) + 2H_2O(l) + 6H^+(aq.) + 6e \leftrightharpoons 2NH_3 \cdot H_2O(aq.)} \tag{4}$$

In this half-reaction of N_2 reduction, the charge transfer of six electrons was required for the activation of one N_2 molecule, and the standard potential for this half reaction of NRR was 0.092 V. The Nernst equation was used to calculate the equilibrium potential of this reaction under these experimental conditions, assuming 1 atm of N_2.[33] In addition, since the concentration of newly produced $NH_3{\cdot}H_2O$ in the electrolyte varied from 0.001×10^{-3} to 0.01×10^{-3} M, the $NH_3{\cdot}H_2O$ concentration was assumed as 0.005×10^{-3} M for calculating the equilibrium potential of this NRR half-reaction

$$E = E^\circ - RT/6F * \ln\left(\left[\mathrm{NH_4OH}\right]^2 / \left[\mathrm{H^+}\right]^6\right) + 0.059\ \mathrm{V} \times \mathrm{pH} = 0.196\ \mathrm{V\ versus\ RHE} \tag{5}$$

Computational and Modeling Methods: In this study, the DFT calculations were conducted with Vienna Ab initio Simulation Package. Projector augmented-wave method and expanded Kohn–Sham (KS) wave functions in plane wave basis were, respectively, employed to describe the core[34] and valence[35] electrons. Electronic exchange was described by generalized gradient approximation and the correlation was described with the Perdew–Burke–Ernzerhof functional.[36] The Brillouin zone was sampled via a $3 \times 3 \times 1$ Monkhorst–Pack *k*-point mesh.[37] An energy cutoff for all the calculations was set at 400 eV, and the force convergence criteria were set lower than 0.05 eV $Å^{-1}$. The energy barriers were calculated using the climbing image nudged elastic band method (Cl-NEB).[38] Since spin-polarization had neglectable influence on this study, it was not included in these results. Entropic corrections were applied to the gas phase N_2 (0.59 eV) and NH_3 (0.60 eV) at a temperature of 298 K.

The Ru SAs/g-C_3N_4 was modeled as one Ru atom bound with the three pyridinic N on a (8×8) g-C_3N_4 surface. To simulate the close-packed surface of the large Ru clusters, a (4×4), four-layer, Ru(0001) slab was modeled. The bottom two layers were held fixed while the two topmost layers were allowed to relax. The reaction free energy profile of the NRR was calculated according to the computational hydrogen electrode method with the energy of proton–electron pair equaled to half of the total energy of H_2 in the gas phase.[39] The H binding energy E_H was calculated using Equation (6)

$$E_\mathrm{H} = E_\mathrm{tot} - E_\mathrm{Site} - \frac{1}{2}E_{\mathrm{H_2}} \tag{6}$$

where E_{tot} is the total energy of the adsorption system, E_{Site} is the total energy of the bare system without adsorbed H, and E_{H_2} is the total energy of a H_2 molecule in vacuum. The free energy of HER (G_H) was calculated by Equation (7) with zero-point energy and entropic corrections[12]

$$G_\mathrm{H} = E_\mathrm{H} + 0.24\ \mathrm{eV} \tag{7}$$

Supporting Information

Supporting Information is available from the Wiley Online Library or from the author.

Acknowledgements

B.Y. and H.L. contributed equally to this work. This work was financially supported by Australian Research Council (ARC) through Discovery Early Career Researcher Award (DE150101306) and Linkage Project (LP160100927), Faculty of Science Strategic Investment Funding 2019 of University of Newcastle, Liaoning Revitalization Talents Program–Pan Deng Scholars (XLYC1802005), Liaoning BaiQianWan Talents Program, the National Science Fund of Liaoning Province for Excellent Young Scholars, and Science and Technology Innovative Talents Support Program of Shenyang (RC180166). The authors also wish to acknowledge financial assistance provided through CSIRO Energy, Australia, and "Shuang Chuang" Fellowship, Fujian, China. H.L. acknowledges the 2017 Hamilton/Schoch Fellowship, 2018 Department Excellence Fellowship, and 2019–2020 University Graduate Continuing Fellowship. The computational work was supported by the Welch Foundation (F-1841) and the Texas Advanced Computing Center.

Conflict of Interest

The authors declare no conflict of interest.

Keywords

ammonia synthesis, g-C_3N_4, hydrogen evolution, single atoms

Received: July 13, 2019
Revised: October 13, 2019
Published online:

[1] a) J. Han, X. Meng, L. Lu, J. Bian, Z. Li, C. Sun, *Adv. Funct. Mater.* **2019**, *29*, 1808872; b) X.-F. Yang, A. Wang, B. Qiao, J. Li, J. Liu, T. Zhang, *Acc. Chem. Res.* **2013**, *46*, 1740.
[2] a) J. Kim, C. W. Roh, S. K. Sahoo, S. Yang, J. Bae, J. W. Han, H. Lee, *Adv. Energy Mater.* **2018**, *8*, 1701476; b) P. Xie, T. Pu, A. Nie, S. Hwang, S. C. Purdy, W. Yu, D. Su, J. T. Miller, C. Wang, *ACS Catal.* **2018**, *8*, 4044.
[3] Y. Peng, Z. Geng, S. Zhao, L. Wang, H. Li, X. Wang, X. Zheng, J. Zhu, Z. Li, R. Si, *Nano Lett.* **2018**, *18*, 3785.
[4] Y. Zhu, W. Sun, W. Chen, T. Cao, Y. Xiong, J. Luo, J. Dong, L. Zheng, J. Zhang, X. Wang, *Adv. Funct. Mater.* **2018**, *28*, 1802167.
[5] C. Lu, J. Yang, S. Wei, S. Bi, Y. Xia, M. Chen, Y. Hou, M. Qiu, C. Yuan, Y. Su, *Adv. Funct. Mater.* **2019**, *29*, 1806884.
[6] a) X. Guo, Y. Zhu, T. Ma, *J. Energy Chem.* **2017**, *26*, 1107; b) H. Wang, L. Wang, Q. Wang, S. Ye, W. Sun, Y. Shao, Z. Jiang,

Q. Qiao, Y. Zhu, P. Song, *Angew. Chem., Int. Ed.* **2018**, *57*, 12360; c) S. Wang, F. Ichihara, H. Pang, H. Chen, J. Ye, *Adv. Funct. Mater.* **2018**, *28*, 1803309.

[7] F. Jiao, B. Xu, *Adv. Mater.* **2018**, *31*, 1805173.

[8] a) Y. Song, D. Johnson, R. Peng, D. K. Hensley, P. V. Bonnesen, L. Liang, J. Huang, F. Yang, F. Zhang, R. Qiao, *Sci. Adv.* **2018**, *4*, e1700336; b) W. Zhou, B. Zhu, Q. Li, T. Ma, S. Hu, C. Griffy-Brown, *Energy Policy* **2010**, *38*, 3701; c) J. G. Chen, R. M. Crooks, L. C. Seefeldt, K. L. Bren, R. M. Bullock, M. Y. Darensbourg, P. L. Holland, B. Hoffman, M. J. Janik, A. K. Jones, *Science* **2018**, *360*, eaar6611; d) M. Falcone, L. Barluzzi, J. Andrez, F. F. Tirani, I. Zivkovic, A. Fabrizio, C. Corminboeuf, K. Severin, M. Mazzanti, *Nat. Chem.* **2019**, *11*, 154.

[9] Z. Geng, Y. Liu, X. Kong, P. Li, K. Li, Z. Liu, J. Du, M. Shu, R. Si, J. Zeng, *Adv. Mater.* **2018**, *30*, 1803498.

[10] S. L. Foster, S. I. P. Bakovic, R. D. Duda, S. Maheshwari, R. D. Milton, S. D. Minteer, M. J. Janik, J. N. Renner, L. F. Greenlee, *Nat. Catal.* **2018**, *1*, 490.

[11] a) H. Tao, C. Choi, L.-X. Ding, Z. Jiang, Z. Han, M. Jia, Q. Fan, Y. Gao, H. Wang, A. W. Robertson, *Chem* **2019**, *5*, 204; b) L. Han, X. Liu, J. Chen, R. Lin, H. Liu, F. Lü, S. Bak, Z. Liang, S. Zhao, E. Stavitski, *Angew. Chem., Int. Ed.* **2019**, *58*, 2321; c) Q. Qin, T. Heil, M. Antonietti, M. Oschatz, *Small Methods* **2018**, *2*, 1800202.

[12] a) Z. Zhuang, Y. Li, Z. Li, F. Lv, Z. Lang, K. Zhao, L. Zhou, L. Moskaleva, S. Guo, L. Mai, *Angew. Chem.* **2018**, *130*, 505; b) C. Han, P. Meng, E. R. Waclawik, C. Zhang, X. H. Li, H. Yang, M. Antonietti, J. Xu, *Angew. Chem., Int. Ed.* **2018**, *57*, 14857; c) G. Gao, Y. Jiao, E. R. Waclawik, A. Du, *J. Am. Chem. Soc.* **2016**, *138*, 6292; d) Y. Zheng, Y. Jiao, Y. Zhu, Q. Cai, A. Vasileff, L. H. Li, Y. Han, Y. Chen, S.-Z. Qiao, *J. Am. Chem. Soc.* **2017**, *139*, 3336.

[13] Y. Wang, X. Wang, M. Antonietti, *Angew. Chem., Int. Ed.* **2012**, *51*, 68.

[14] F. Lü, S. Zhao, R. Guo, J. He, X. Peng, H. Bao, J. Fu, L. Han, G. Qi, J. Luo, *Nano Energy* **2019**, *61*, 420.

[15] X. Wang, W. Wang, M. Qiao, G. Wu, W. Chen, T. Yuan, Q. Xu, M. Chen, Y. Zhang, X. Wang, *Sci. Bull.* **2018**, *63*, 1246.

[16] C. He, Z.-Y. Wu, L. Zhao, M. Ming, Y. Zhang, Y. Yi, J.-S. Hu, *ACS Catal.* **2019**, *9*, 7311.

[17] Y. Wang, X. Cui, J. Zhao, G. Jia, L. Gu, Q. Zhang, L. Meng, Z. Shi, L. Zheng, C. Wang, *ACS Catal.* **2019**, *9*, 336.

[18] M. Wang, S. Liu, T. Qian, J. Liu, J. Zhou, H. Ji, J. Xiong, J. Zhong, C. Yan, *Nat. Commun.* **2019**, *10*, 341.

[19] J. Liu, Y. Liu, N. Liu, Y. Han, X. Zhang, H. Huang, Y. Lifshitz, S.-T. Lee, J. Zhong, Z. Kang, *Science* **2015**, *347*, 970.

[20] F. Wang, P. Chen, Y. Feng, Z. Xie, Y. Liu, Y. Su, Q. Zhang, Y. Wang, K. Yao, W. Lv, *Appl. Catal., B* **2017**, *207*, 103.

[21] D. Wang, L. M. Azofra, M. Harb, L. Cavallo, X. Zhang, B. H. Suryanto, D. R. MacFarlane, *ChemSusChem* **2018**, *11*, 3416.

[22] a) Y. Peng, W. Pan, N. Wang, J. E. Lu, S. Chen, *ChemSusChem* **2018**, *11*, 130; b) S. Cao, J. Jiang, B. Zhu, J. Yu, *Phys. Chem. Chem. Phys.* **2016**, *18*, 19457.

[23] S. Yang, Y. Gong, J. Zhang, L. Zhan, L. Ma, Z. Fang, R. Vajtai, X. Wang, P. M. Ajayan, *Adv. Mater.* **2013**, *25*, 2452.

[24] X. Wu, C. Liu, X. Li, X. Zhang, C. Wang, Y. Liu, *Mater. Sci. Semicond. Process.* **2015**, *32*, 76.

[25] S.-A. Chen, Y.-C. Liang, K.-T. Lu, C.-W. Pao, J.-F. Lee, T.-L. Lin, J.-M. Chen, *Phys. Chem. Chem. Phys.* **2014**, *16*, 3939.

[26] W. Kong, R. Zhang, X. Zhang, L. Ji, G. Yu, T. Wang, Y. Luo, X. Shi, Y. Xu, X. Sun, *Nanoscale* **2019**, *11*, 19274.

[27] K. Chu, Y.-P. Liu, J. Wang, H. Zhang, *ACS Appl. Energy Mater.* **2019**, *2*, 2288.

[28] Y. Luo, G.-F. Chen, L. Ding, X. Chen, L.-X. Ding, H. Wang, *Joule* **2019**, *3*, 279.

[29] S. Back, Y. Jung, *Phys. Chem. Chem. Phys.* **2016**, *18*, 9161.

[30] E. Skulason, T. Bligaard, S. Gudmundsdóttir, F. Studt, J. Rossmeisl, F. Abild-Pedersen, T. Vegge, H. Jonsson, J. K. Nørskov, *Phys. Chem. Chem. Phys.* **2012**, *14*, 1235.

[31] a) H. Li, K. Shin, G. Henkelman, *J. Chem. Phys.* **2018**, *149*, 174705; b) H. Li, E. J. Evans Jr., C. B. Mullins, G. Henkelman, *J. Phys. Chem. C* **2018**, *122*, 22024; c) H. Li, L. Luo, P. Kunal, C. S. Bonifacio, Z. Duan, J. C. Yang, S. M. Humphrey, R. M. Crooks, G. Henkelman, *J. Phys. Chem. C* **2018**, *122*, 2712; d) H. Li, G. Henkelman, *J. Phys. Chem. C* **2017**, *121*, 27504.

[32] H. Li, W. Chai, G. Henkelman, *J. Mater. Chem. A* **2019**, *7*, 23868.

[33] J. Wang, L. Yu, L. Hu, G. Chen, H. Xin, X. Feng, *Nat. Commun.* **2018**, *9*, 1795.

[34] P. E. Blöchl, *Phys. Rev. B* **1994**, *50*, 17953.

[35] J. A. Pople, P. M. Gill, B. G. Johnson, *Chem. Phys. Lett.* **1992**, *199*, 557.

[36] J. P. Perdew, K. Burke, M. Ernzerhof, *Phys. Rev. Lett.* **1996**, *77*, 3865.

[37] H. J. Monkhorst, J. D. Pack, *Phys. Rev. B* **1976**, *13*, 5188.

[38] G. Henkelman, B. P. Uberuaga, H. Jónsson, *J. Chem. Phys.* **2000**, *113*, 9901.

[39] J. K. Nørskov, J. Rossmeisl, A. Logadottir, L. Lindqvist, J. R. Kitchin, T. Bligaard, H. Jonsson, *J. Phys. Chem. B* **2004**, *108*, 17886.